

Data Fusion for Catheter Tracking using Kalman Filtering: Applications in Robot-Assisted Catheter Insertion

Mahdi Azizian^{a,c} and Rajni Patel^{a,b,c}

^aDept. of Electrical and Computer Eng. ^bDept. of Surgery, University of Western Ontario

^cCanadian Surgical Technologies & Advanced Robotics (CSTAR), London, Ontario, Canada

ABSTRACT

X-ray image guided angioplasty is a minimally invasive procedure that involves the insertion of a catheter into a blood vessel to remove blockages to blood flow. There are several issues associated with conventional angioplasty which cause risks for the patient (damage to blood vessels, dislodging plaques, etc.) and difficulties for the clinician (X-ray exposure, fatigue, etc.). Autonomous or semi-autonomous robot-assisted catheter insertion is a solution that can reduce these problems substantially. To perform autonomous catheter insertion, closed-loop position control of the distal tip of the catheter is required during insertion. Therefore accurate real-time position feedback is needed for this purpose. We have developed a real-time image processing algorithm for catheter tip position tracking which has an acceptable performance but is sensitive to X-ray image artifacts caused by bones and dense tissues. A magnetic tracking system (MTS) is another modality that has also been used for catheter tip position tracking, but it is sensitive to external electromagnetic interferences and ferromagnetic material. Combining the measurement data provided by both imaging and magnetic sensors can compensate for the deficiencies of each and can also improve the robustness of catheter tip position tracking. We have developed a Kalman filter based sensor fusion scheme to overcome deficiencies of both of these methods and create a reliable real-time tracking of a catheter tip. Experiments have been performed by inserting a guide catheter into a model of the vasculature. The method has been tested in presence of occlusion in the images and also electromagnetic interference.

Keywords: Data Fusion, Catheter Insertion, Image-based Tracking, Magnetic Tracking, Kalman Filtering

1. INTRODUCTION

X-ray guided angioplasty is a minimally invasive procedure that involves the insertion of a catheter into a blood vessel to remove blockages to blood flow. There are several issues associated with conventional angioplasty which cause risks for the patient and difficulties for the clinician. For the patient, there is a risk of damage to blood vessels due to repeated insertions or dislodging of plaque. There are also risks for the clinicians due to long procedure times while working in an environment with X-rays and a high-level of fatigue resulting from wearing heavy lead aprons. Therefore there is a need to develop technology for a more accurate, safer and more reliable approach for catheter insertion that can reduce the potential risk of injury to patients and radiation exposure and discomfort to clinicians. Autonomous or semi-autonomous robot-assisted catheter insertion is a solution that can reduce these problems substantially.¹ To perform autonomous catheter insertion, closed-loop position control of the distal tip of the catheter is required during insertion. Therefore accurate real-time position feedback is needed for this purpose. We have developed a real-time image-processing algorithm for catheter tip position tracking.^{1,2} The performance of the image-based tracking algorithm has been shown to be acceptable, however it has a major drawback: It is sensitive to X-ray image artifacts caused by bones and dense tissues. A magnetic tracking system (MTS) is another modality that has also been used for catheter tip position tracking.³ The performance of MTS is good within certain limits; however it has a major deficiency: it is sensitive to external interferences produced by ferrous metals and other magnetic fields. Combining the measurement data provided by both imaging and magnetic sensors can compensate for the deficiencies of each and can also improve the robustness of catheter tip position tracking.

Further author information: Mahdi Azizian: E-mail: mazizian@uwo.ca, Rajni Patel: E-mail: rvpatel@uwo.ca, Tel: +1(519)661-2111-Ext. 36618. Room B-700 (CSTAR), University Hospital, 339 Windermere Road, London, ON, Canada, N6A 5A5.

Medical Imaging 2011: Visualization, Image-Guided Procedures, and Modeling,
edited by Kenneth H. Wong, David R. Holmes III, Proc. of SPIE Vol. 7964, 796413
© 2011 SPIE · CCC code: 1605-7422/11/\$18 · doi: 10.1117/12.878148

Proc. of SPIE Vol. 7964 796413-1

Multisensor data fusion has a wide range of applications in different areas. Sensory information from different sources can be applied to extract the maximum amount of information possible about the sensed object(s) (e.g. catheter) under various conditions (e.g. in case of an occlusion), in real time. This will result in higher performance and reliability in presence of uncertain sensory data. It may also help in achieving higher data rates as a result of sampling at different time instants. The purpose of data fusion is to produce a model or representation of a system from a set of independent data sources, from which a single view or perception of the system is detected; Normally, a state-space model of the process is used for this purpose. The combination of information from different sensors and the subsequent state estimation should result in reduced uncertainty. The data fusion algorithm should be able to handle multiple observations and multiple sensor, and at the same time it should be able to consider faults in sensory data. A common application of data fusion techniques is the estimation of target position/velocity information from multiple measurements from a single or multiple sensor(s). Two essential processes are involved in the derivation of position/velocity: (a) data association and (b) state estimation. Data association is done to distinguish between the true information and clutter. State estimation refers to optimal estimation of the variables, e.g., the position and velocity of the target, using the observation data after the data association process has been performed.⁴

Kalman filtering has found widespread application in data fusion problems.⁴ Kalman filtering based data fusion models can be classified into two categories:⁵ (a) measurement level fusion and (b) state level fusion. Measurement level fusion methods are further divided into two subcategories: (1) augmented observation and (2) minimum mean-squared measurement estimate fusion. State level fusion techniques are basically different variations of Bar-Shalom's track to track fusion method.^{5,6}

To combine the data from the two different sources, the coordinates of the MTS and the imaging system need to be registered. An off-line registration algorithm has been developed that finds the transformation between the coordinates of the two sensors. To compensate for the nonlinearities of the imaging system (e.g. radial distortion), a camera calibration method has been used that finds the intrinsic parameters of the imaging system.¹ A Kalman filter has been developed which uses the measurements of both sensors to provide accurate and reliable position feedback. The results show robust and accurate tracking regardless of occlusions in the images or interferences in the magnetic field. It also provides a higher sampling rate by interpolating the estimated data. This method provides accurate and reliable position feedback that can be used by a robotic system to control the catheter tip position in real-time.^{7,8}

In Section 2 we describe the sensors which we have used for tracking the tip of the catheter and also discuss the algorithm used for registering these two sensors as they have different coordinate systems. Section 3 describes a simple motion model for the tip of the catheter. This model is used for the design of the Kalman filter for data fusion as described in Section 4. In Section 5, the results and implementation issues are described. Section 6 concludes the paper with some suggestions for future work.

2. CATHETER TIP TRACKING SENSORS

There are several methods for detecting the tip position of the catheter inside blood vessels in real time. One method uses image processing algorithms to track the tip of the catheter in X-ray cine-fluoroscopic images. This method can achieve sampling rates of up to 30Hz. More details are given in Section 2.1. Another method applies magnetic tracking systems to track the tip of the catheter.³ This method can achieve up to 40Hz, for example, using the Aurora⁹ magnetic measurement system (Northern Digital Inc., Waterloo, ON, CA). A brief description of this system is included in Section 2.2. The experimental setup is shown in Figure 1.

2.1 Image-based Tracking

In our laboratory tests, we have used a fire-wire digital camera to simulate X-ray fluoroscopy. The camera captures 640×480 pixel 8-bit gray scale images at a rate of 30fps while the catheter is inserted into the test-bed (Figure 1(a)). We have also tested the system on a GE OEC 9900 Elite C-Arm with a more realistic model of vasculature (Figure 1(b)). The maximum frame rate is limited by two bottlenecks. One is the time resolution of the imaging device (e.g. X-ray fluoroscopy) and the other is the time required for processing a captured frame. Most of the modern X-ray fluoroscopy systems have a time resolution up to 30 frames per second¹⁰ and a spatial resolution of 640×480 when the images are captured through the analog video output; therefore the selection of

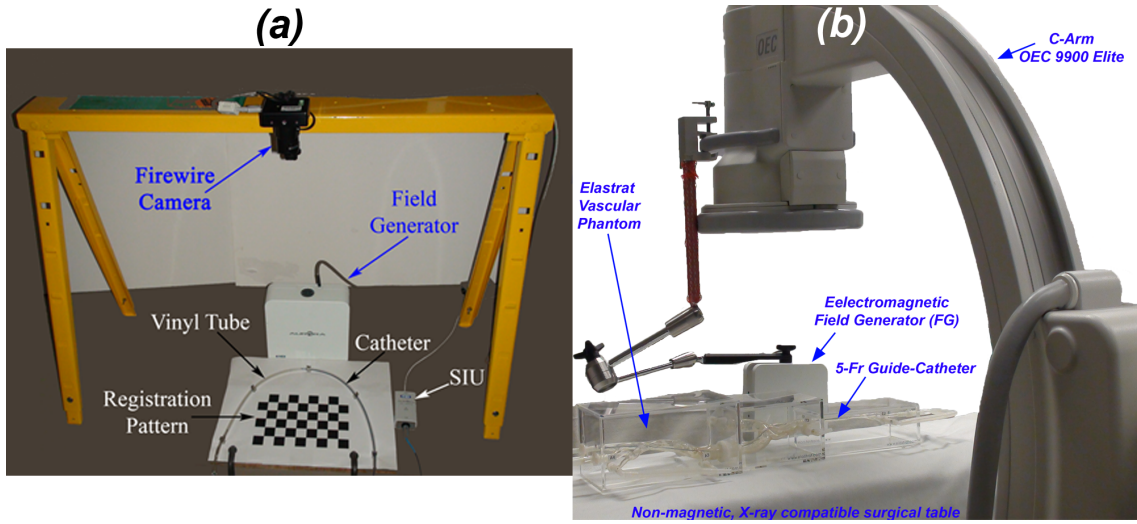


Figure 1. (a) Simplistic experimental setup for validation of the results, (b) Realistic experimental setup.

this firewire camera is realistic. The images obtained from this camera are similar to X-ray fluoroscopic images in terms of brightness, contrast and frame capture rate.

2.1.1 Off-line Camera Calibration

Fluoroscopic images obtained by an X-ray image intensifier (XRII) undergo geometric distortion as a systematic error. The geometric distortions (mainly pincushion distortion and sigmoidal distortion) have three main sources, (a) the projection of the X-ray beam onto the curved input surface of the XRRII, (b) the deflection of the electrons inside the XRRII caused by any external magnetic field, and (c) the significant frame deformation when the C-arm rotates.¹¹ Correction of such images can be done using a radio-opaque grid of lines or points with known spatial coordinates. The same phenomenon as in (a), rules over the cameras which present a radial distortion to the images. To remove this radial distortion and to find the perspective parameters, we have used Zhang's method¹² for calibration. We have measured the root mean squared calibration error as 0.37698 pixels along the width of the image and 0.24777 pixels along the height of the image which results in an overall RMS error of 0.4511 pixels.

2.1.2 Roadmap Generation

A flowchart of the roadmap (mask) generation algorithm¹ is shown in Figure 2. In the clinical case, a contrast agent is injected into the vascular system to make the blood vessels visible under X-ray images. The contrast media will help to improve the contrast-to-noise ratio (CNR). This will help in segmentation of the vascular tree.¹³ To extract the centerlines of the tubes (vessels), a least-squares error algorithm is applied to fit piecewise polynomials to different segments of the tubes (vessels). We assume an N^{th} order implicit polynomial equation in x and y coordinates as $f(x, y) = 0$ where:

$$f(x, y) = \sum_{n=0}^N \sum_{i=0}^n (c_{i,n-i} x^i y^{n-i}) \quad (1)$$

The polynomial equations are used in the motion model for the catheter tip as described in Section 3. In this application we use a piecewise sixth degree polynomial. The variable which we use for robot-assisted catheter insertion control is the displacement of the catheter tip along the tube; Therefore the centerline is required to calculate the displacement of the catheter tip along the tube. This is important especially when there is a curvature as shown in Figure 2 (right-hand side).

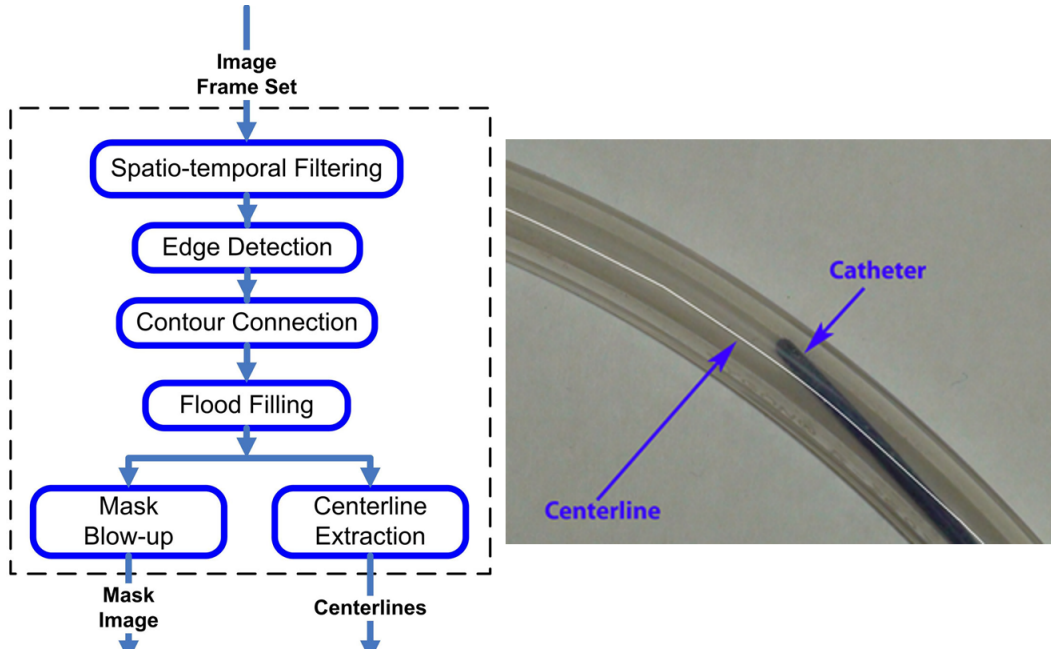


Figure 2. Flowchart for the roadmap (mask image) generation is shown on the left and the extracted centerline is shown on the right. As shown in the image, the catheter may have a deflection with respect to the centerline of the tubes because of the curvatures.

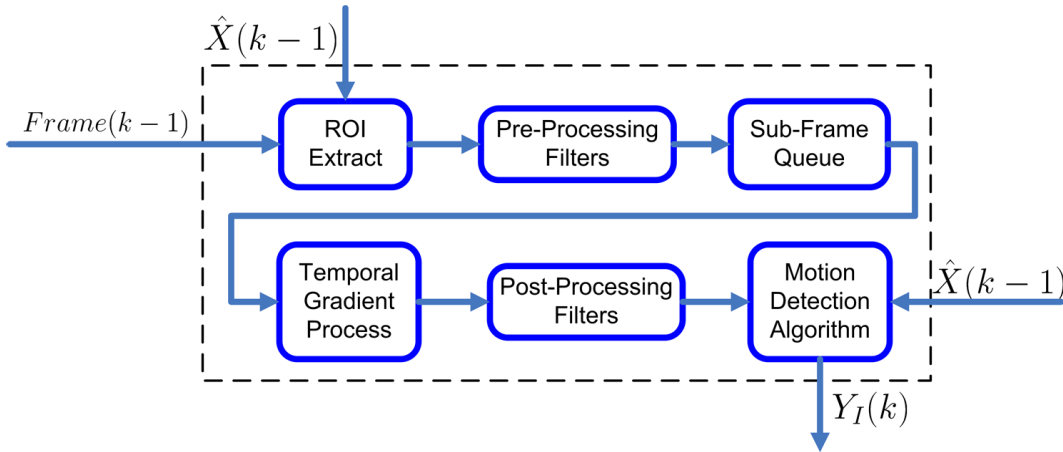


Figure 3. Flowchart of the image-based tracking algorithm

2.1.3 Tracking the tip of the catheter

The images are processed using a real-time algorithm to track the tip of the catheter.² The flowchart for real-time tracking is shown in Figure 3. The algorithm mainly consists of the following steps:

- The video stream consists of a stream of frames grabbed by the camera with a rate of up to 30fps.
- The ROI extraction is done around the previous valid estimation of the catheter tip position.
- The pre-processing filter block consists of a set of filters for suppressing noise, masking the image and improving the contrast of the image.
- The frame queue is an image buffer structure which provides the appropriate input for the temporal gradient algorithm.

- The temporal gradient algorithm takes the time gradient of the images in the frame queue.
- The post-gradient filters suppress the noise in the gradient image and make it useful for the motion detection algorithm.
- The motion detection algorithm searches for the catheter tip in a neighborhood around the previously known position of the catheter tip. The neighborhood is a rectangle which extends more to the previously known direction of motion.
- When the new position of the catheter tip is detected, the result is given to the data fusion algorithm.

2.2 Magnetic Tracking System

We have used a 5-DOF magnetic tracking sensor, implemented at the tip of the catheter to detect the tip position. The Aurora magnetic tracking system consists of sensor coils and a sensor interface unit (SIU) for each sensor coil, a field generator device and a system control unit. The system control unit is connected to the computer through an RS-232 link; It also provides the power for the field generator. Sensor coils are connected to the system control unit via sensor interface units. The 5-DOF position/orientation of a sensor coil can be detected when it is placed in a $500mm \times 500mm \times 500mm$ cubic volume in front of the field generator. The RMS error for this sensor is in the range of 0.9mm to 1.3mm depending on the location of the sensor coil with respect to the field generator. This sensor is able to measure 3-DOF position and 2-DOF orientation of the catheter tip.

2.2.1 Offset Calibration

The magnetic sensor is usually not located at the tip of the catheter and has a fixed distance from the tip. An off-line calibration process needs to be performed to measure this offset. The value obtained for the offset is then used to calculate the actual position of the catheter tip in real-time. Zhang et al.¹⁴ have designed a simple pivot calibration algorithm. We have used this pivot calibration algorithm with three different points in the workspace and obtaining 1000 samples for each point, by fixing the tip of the catheter at that point and changing the orientation. The results show an offset of $17.7323mm$ with an RMS error of $0.9973mm$.

2.3 Registration of the two sensors

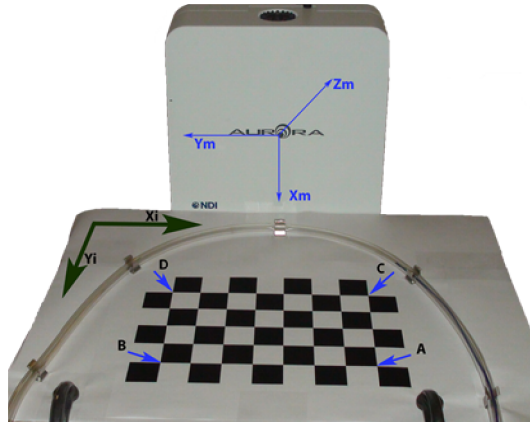


Figure 4. Registration pattern; The coordinate system of the camera is shown by X_i , Y_i and the coordinate system of the magnetic tracking system is shown by X_m , Y_m , Z_m . The four corner points are marked as \mathcal{A} , \mathcal{B} , \mathcal{C} and \mathcal{D}

A planar chessboard pattern with known size, as shown in Figure 4, is used to register the image tracking and the magnetic tracking coordinate systems. The registration process is as follows:

- The coordinates of the four outer corners of the non-planar pattern (as marked by \mathcal{A} , \mathcal{B} , \mathcal{C} and \mathcal{D} in Figure 4) are obtained by means of the magnetic tracking sensor and are logged into the computer. Three of these points are enough to obtain the geometry of the pattern and the fourth point is only used to reduce the errors.

- The registration algorithm calculates the 3D coordinates of the inner corners of the pattern using the coordinates of outer corners and the pre-known geometry of the pattern. The set of the coordinates obtained from this process is denoted by M .
- An image of the pattern (I) is obtained from the camera and undistorted using the distortion parameters obtained in the offline camera calibration procedure. We call the undistorted image as I' .
- A pattern recognition algorithm is used to find the coordinates of all the corner points in the undistorted image I' . We denote the set of corner points obtained from I' as P' .
- The obtained set of points P' is rearranged corresponding to the order of the points in M ; The rearranged matrix is called P .
- A least-squares method is applied to find a 2D-3D transformation that maps the 2D coordinates of points in the image plane to the 3D coordinates of the points in the magnetic tracking system.

We take $P = \{(\xi_k, \eta_k) | k = 1 \dots n\}$ and $M = \{(x_k, y_k, z_k) | k = 1 \dots n\}$ where n is the number of points used for registration. We also define Q and R matrices as follows:

$$Q = \begin{bmatrix} \xi_1 & \dots & \xi_n \\ \eta_1 & \dots & \eta_n \end{bmatrix}, R = \begin{bmatrix} x_1 & \dots & x_n \\ y_1 & \dots & y_n \\ z_1 & \dots & z_n \\ 1 & \dots & 1 \end{bmatrix}$$

Now we solve the following optimization problem for the 2×4 matrix T , $\min_T \|TR - Q\|$. This optimization problem will have a unique solution for an appropriate number of points (at least four points). As our pattern (shown in Figure 4) has 5×8 points located on the same plane, it should result in a unique optimal solution. We call this solution, T_o . The matrix T_o is then used for registration of the undistorted image plane coordinates to the coordinates of the magnetic tracking system. A point $p = [x \ y \ z]^T$ detected by the magnetic tracking system, will be corresponding to the point $q = [\xi \ \eta]^T$ in the undistorted image plane, where $q = T_o [p^T \ 1]^T$. This registration method is an efficient algorithm developed for this application based on similar methods that can be found in the computer vision literature.¹⁵ In a clinical application, the registration process would be modified by using a pattern that can be recognized in the X-ray images. Krueger et al.¹⁶ have developed a 2D-3D registration scheme by attaching a magnetic tracking system to the C-arm. We have measured the RMS registration error and it has an average value of $1.1269mm$. For X-ray fluoroscopic images, we can use a wire grid with pre-known geometry. This wire grid can also be used for calibration.¹¹

3. MODELING THE CATHETER TIP MOTION

The catheter is usually moved slowly and without sudden velocity changes to avoid rupturing the blood vessels; Therefore we can ignore the acceleration and develop the motion model at velocity level. The catheter tip motion model for real-time tracking can be described as a state-space equation:¹⁷

$$\begin{cases} P_t(k+1) = P_t(k) + V_t(k) + \omega_P(k) \\ V_t(k+1) = V_t(k) + \omega_V(k) \end{cases} \quad (2)$$

and the augmented output equations for our application can be modeled as:

$$\begin{cases} P_I(k) = P_t(k) + \nu_I(k) \\ P_M(k) = P_t(k) + \nu_M(k) \end{cases} \quad (3)$$

where $P_t(k)$ and $V_t(k)$ are the states of the system at time instant k , $P_t(k) = [x_t(k) \ y_t(k)]^T$ is the position of the distal tip of the catheter in the two dimensional undistorted image plane and $V_t(k) = [v_{x_t}(k) \ v_{y_t}(k)]^T$ is the 2D displacement vector, at the time instant k ; $\omega_P(\cdot)$, $\omega_V(\cdot)$ and $\nu_I(\cdot)$, $\nu_M(\cdot)$ are independent zero mean white Gaussian two dimensional random processes which characterize the process noise and measurement noise respectively.

We also need to calculate the actual catheter depth inside the vasculature. To calculate this variable, we integrate the catheter tip displacements along the centerline of the tube/vessel over the time samples. The depth of the catheter inserted into the vasculature is then used in catheter tip position control by the robot client. $V_t(k)$ is the displacement vector for the catheter tip at the time instant k , but it may have a deflection around the centerline of the vessel, specially when it is near the curvatures. This is shown on the right hand side in Figure 2. To obtain the amount of displacement along the centerline of the tubes/vessels, we use the projection of the displacement vector $V_t(k)$ on the unit vector along the centerline at that point. The direction of the unit vector is chosen to point forward to the direction of insertion, this helps to distinguish whether the catheter is being pushed in or being pulled out. The unit vector $D(\cdot)$ is a function of the current position of the catheter tip, $P_t(k)$, and depends on the a priori knowledge of the geometry of the vasculature obtained in Section 2.1.2.

$$s(k+1) = s(k) + \langle V_t(k), D(P_t(k)) \rangle \quad (4)$$

where $\langle \cdot, \cdot \rangle$ represents the inner product of two vectors. The variable $s(\cdot)$ is used by the robot client to control the catheter tip position.¹

4. DATA FUSION ALGORITHM DESIGN

We have used Kalman-filter based data fusion at the measurement level which provides optimal tracking compared to the sub-optimal tracking performance of Bar-Shalom's method.⁵ The fusion is performed at the observation level and as we have similar sensors (i.e., the sensors measure the same variables), the performance will be equivalent to the performance provided by the minimum mean-squared measurement estimate fusion.⁵ The structure of the Kalman-filter based data fusion is shown in Figure 5.

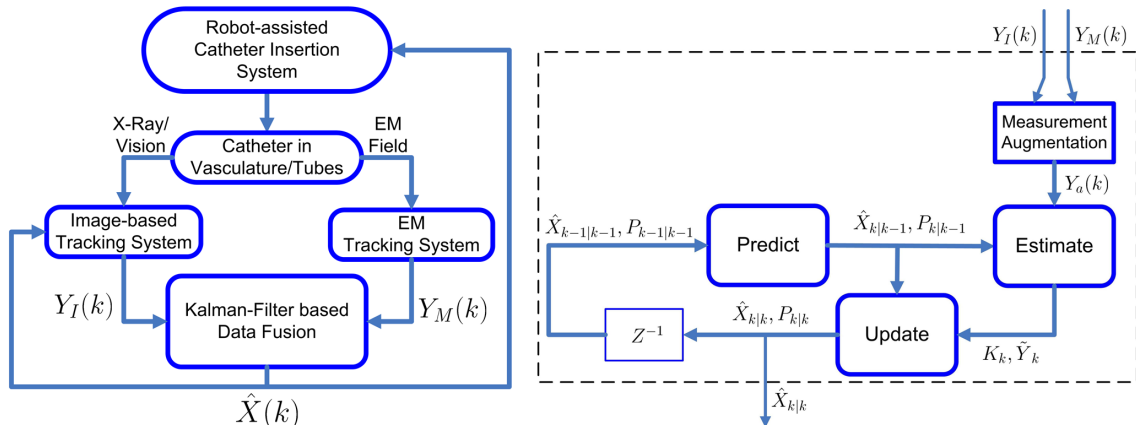


Figure 5. Flowcharts for the overall data fusion (Left) and the Kalman-filter based data fusion (Right).

The augmented state-space equations for the system can be described as:

$$\begin{cases} X_k = \mathcal{F}X_{k-1} + \omega_{k-1} \\ Y_k = \mathcal{C}X_k + \nu_k \end{cases} \quad (5)$$

where $X_k = [P_t^T(k), \ V_t^T(k)]^T$ is the system state and $Y_k = [P_I^T(k), \ P_M^T(k)]^T$ is the augmented system output at time instant k . Using Equations (2) and (3), we obtain:

$$\mathcal{F} = \begin{bmatrix} I_{2 \times 2} & I_{2 \times 2} \\ 0_{2 \times 2} & I_{2 \times 2} \end{bmatrix}, \quad \mathcal{C} = \begin{bmatrix} I_{2 \times 2} & 0_{2 \times 2} \\ I_{2 \times 2} & 0_{2 \times 2} \end{bmatrix} \quad (6)$$

where $I_{2 \times 2}$ is the 2×2 identity matrix. The process noise is $\omega(k) = [\omega_P^T(k), \omega_V^T(k)]^T$, the measurement noise is $\nu(k) = [\nu_P^T(k), \nu_V^T(k)]^T$ and the process and measurement noise covariances are Q_k and R_k respectively.

The Kalman filter process performs data fusion using the augmented measurements as shown in Figure 5. The three steps of Kalman filtering, including prediction, estimation and updating are formulated as follows:¹⁷

- Predict the state and its covariance:

$$\begin{aligned} - \hat{X}_{k|k-1} &= \mathcal{F}\hat{X}_{k-1|k-1} \\ - P_{k|k-1} &= \mathcal{F}P_{k-1|k-1}\mathcal{F}^T + Q_{k-1} \end{aligned}$$

- Estimate the innovation, its covariance and the optimal Kalman gain, based on the prediction:

$$\begin{aligned} - \tilde{Y}_k &= Y_a(k) - \mathcal{C}\hat{X}_{k|k-1} \\ - S_k &= \mathcal{C}P_{k|k-1}\mathcal{C}^T + R_k \\ - K_k &= P_{k|k-1}\mathcal{C}^T S_k^{-1} \end{aligned}$$

- Update the state and its covariance:

$$\begin{aligned} - \hat{X}_{k|k} &= \hat{X}_{k|k-1} + K_k\tilde{Y}_k \\ - P_{k|k} &= (I - K_k\mathcal{C})P_{k|k-1} \end{aligned}$$

where $P_{k|k} = \text{cov}(X_k - \hat{X}_{k|k})$, $P_{k|k-1} = \text{cov}(X_k - \hat{X}_{k|k-1})$ and $S_k = \text{cov}(\tilde{Y}_k)$.

5. IMPLEMENTATION AND RESULTS

We have used image-based tracking and magnetic tracking of the tip position of a catheter at rates of $30Hz$ and $40Hz$, respectively. A multi-threaded application has been developed to perform the image-based tracking and capture the magnetic tracking data as well as the Kalman filtering, in real time. The image processing thread is performed asynchronously whenever a new frame is grabbed; The magnetic sensor measurement is updated in the same way. The Kalman filtering is run synchronously every $3 ms$, the robot client is controlled at the same rate.¹ As the catheter tip position measurement is done in a lower rate than the Kalman filter update rate, we have used a zero-order hold to match the lower rate with the higher rate, i.e., the last valid measurement is used in each iteration of the Kalman filter update. The initial value for the system state X_0 is set to $[x_0, y_0, 0.0, 0.0]^T$ where (x_0, y_0) is the position of the start point (in the undistorted image place coordinates), which is the point where image-based tracking and data fusion start working. The initial state covariance P_0 is set to $\text{diag}(1, 1, .01, .01)$. The process noise covariance matrix is assumed to be constant but the measurement noise covariance is varied during the process; The noise covariance for the magnetic tracking sensor is increased whenever it is unable to provide valid measurement data and generates a data missing error.

Three sets of experiments are performed to evaluate the performance of the data fusion scheme:

1. In the first experiment set, all the conditions are normal, i.e., there is no major occlusion in the camera's view and there is no major electromagnetic interference within the working area of the MTS. The results are shown in Table 1. and Figure 6. As seen in Table 1, the standard deviation of the difference between the estimated value and each of the measured values is less than the standard deviation of the difference between the data from two sensors; This means that the uncertainty has decreased due to data fusion.

x -coordinate	$\text{std}(x_I - x_M)$	$\text{std}(x_M - \hat{x})$	$\text{std}(x_I - \hat{x})$
Values	5.0523	3.7553	2.3331
Percentage	100	74.3285	46.1792
y -coordinate	$\text{std}(y_I - y_M)$	$\text{std}(y_M - \hat{y})$	$\text{std}(y_I - \hat{y})$
Values	5.0251	3.8876	2.4971
Percentage	100	77.3638	49.6935

Table 1. Tracking and data fusion results in normal conditions

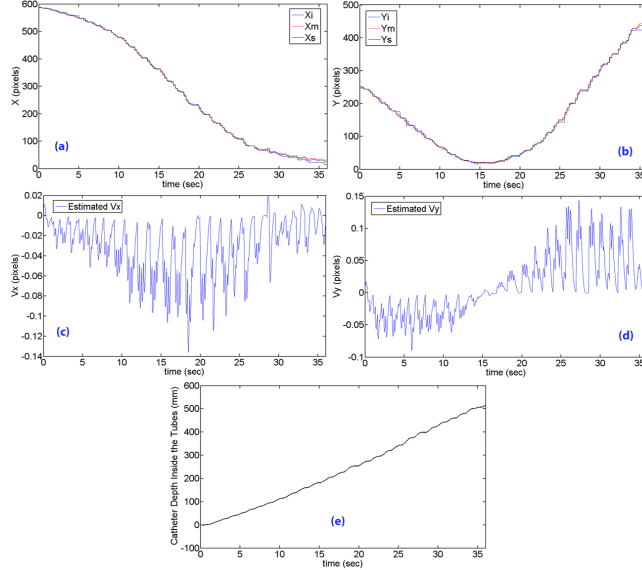


Figure 6. Normal image and magnetic tracking

2. In the second experiment set, all the conditions are normal except that there are considerable occlusions at two different regions (as shown in Figure 7(f)-left), i.e., the view is totally blocked when the catheter is within these regions. As a result, the image-based tracking fails to detect the catheter tip position in these areas. The results are shown in Table 2 and Figure 7-left. As seen in Table 2, the standard deviation of the difference between the estimated value and each of the measured values is less than the standard deviation of the difference between the data from the two sensors; This means that the uncertainty has decreased due to data fusion although the image-based tracking had a major failure twice during the experiment. As seen in Figure 7(e)-left, the estimated catheter insertion depth is not affected by the failure of the image-based tracking sensor.
3. In the third experiment set, all the conditions are normal except that there is considerable amount of electromagnetic interference (EMI). EMI is intentionally created by putting a wire carrying AC current, near the testbed as shown in Figure 7(f)-right. The MTS becomes very noisy when it approaches this area and loses tracking within this region. The results are shown in Table 3 and Figure 7-right. As seen in

x -coordinate	$\text{std}(x_I - x_M)$	$\text{std}(x_M - \hat{x})$	$\text{std}(x_I - \hat{x})$
Values	7.0261	4.8755	2.6704
Percentage	100	69.3907	38.0063
y -coordinate	$\text{std}(y_I - y_M)$	$\text{std}(y_M - \hat{y})$	$\text{std}(y_I - \hat{y})$
Values	6.8302	4.7697	2.6443
Percentage	100	69.8324	38.7149

Table 2. Tracking and data fusion results in case of occlusion

Table 3, the uncertainty has decreased due to data fusion although the magnetic tracking system had a major failure during the experiment. As seen in Figure 7(e)-left, the estimated catheter insertion depth is not affected by the failure of the magnetic tracking sensor.

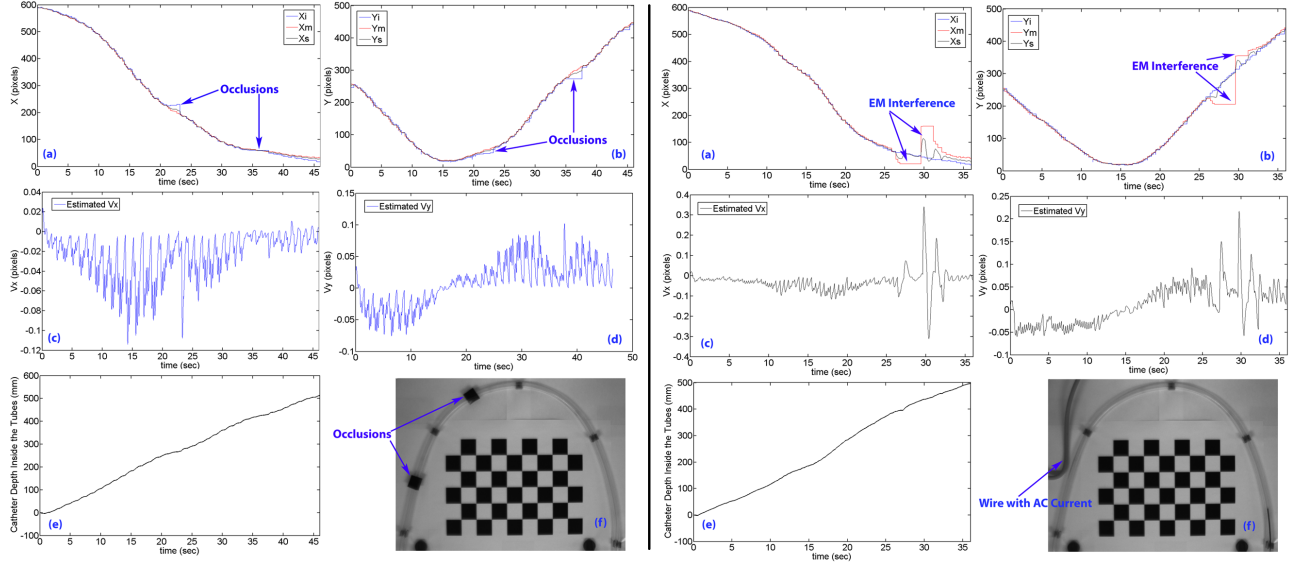


Figure 7. Left: Image and magnetic tracking in case of occlusion. Right: Image and magnetic tracking in case of EM interference.

x -coordinate	$\text{std}(x_I - x_M)$	$\text{std}(x_M - \hat{x})$	$\text{std}(x_I - \hat{x})$
Values	28.4498	10.0257	23.4819
Percentage	100	35.2400	82.5379
y -coordinate	$\text{std}(y_I - y_M)$	$\text{std}(y_M - \hat{y})$	$\text{std}(y_I - \hat{y})$
Values	22.2869	5.3636	20.1194
Percentage	100	24.0662	90.2747

Table 3. Tracking and data fusion results in case of EM interference

6. CONCLUSIONS AND FUTURE WORK

In this paper we have introduced a Kalman filter for data fusion of image-based and magnetic tracking systems in a catheter insertion application. The results indicate reduced uncertainty in the estimated data. The standard deviation of the difference between the image-based and magnetic tracking data, represents a measure of the uncertainty of the measured variables (x and y). The standard deviations of the differences between the measurements of each sensor and the corresponding estimated variable, show decreased uncertainty after data fusion. The percentage of the uncertainty after data fusion to the uncertainty before data fusion is shown in the third and sixth rows of the Tables. 1, 2 and 3 for different experiments with different conditions.

The data fusion scheme provides better estimation with more accuracy and less uncertainty compared to each of the sensors individually. It also provides an estimation of the displacement in each direction (x and y) which is then used to estimate the catheter insertion depth. The estimate of the insertion depth is then used to control the catheter tip position in the vasculature.¹ The estimator can also provide higher-frequency feedback compared to each of the sensors, by interpolating the data. This would be very useful for efficient catheter tip position control using robot-assisted insertion. As part of our future work, we are developing an adaptive data fusion scheme which can update the noise characteristics ($Q(k)$ and $R(k)$) based on the varying errors in the observed values. This will help to penalize the sensor with more uncertainty and give advantage to the sensor with less uncertainty.

Acknowledgments

The work of M. Azizian and R.V. Patel was supported by funds from the Natural Sciences and Engineering Research Council (NSERC) of Canada under grant RGPIN-1345 (R.V. Patel). Financial support for M. Azizian was also provided by an NSERC Alexander Graham Bell Canada Graduate Scholarship.

REFERENCES

1. J. Jayender, M. Azizian, and R. V. Patel, "Autonomous image-guided robot-assisted active catheter insertion," *IEEE Transactions on Robotics* **24**(4), pp. 858–871, 2008.
2. M. Azizian, J. Jayender, and R. V. Patel, "Image processing algorithms for real-time tracking and control of an active catheter," in *European Control Conference (ECC)*, 2007.
3. C. Tercero, S. Ikeda, T. Uchiyama, T. Fukuda, F. Arai, Y. Okada, Y. Ono, R. Hattori, T. Yamamoto, M. Negoro, and I. Takahashi, "Autonomous catheter insertion system using magnetic motion capture sensor for endovascular surgery," *International Journal of Medical Robotics and Computer Assisted Surgery* **3**(1), pp. 52–58, 2006.
4. H. B. Mitchell, *Multi-Sensor Data Fusion: An Introduction*, Springer, 2007.
5. J. B. Gao and C. J. Harris, "Some remarks on kalman filters for the multisensor fusion," *Information Fusion* **3**, pp. 191–201, September 2002.
6. Y. Bar-Shalom and L. Campo, "The effect of the common process noise on the two-sensor fused-track covariance," *IEEE Transactions on Aerospace Electronic Systems* **22**, pp. 803–805, November 1986.
7. J. Jayender, M. Azizian, and R. Patel, "Autonomous robot-assisted active catheter insertion using image guidance," in *IEEE/RSJ International Conference on Intelligent Robots and Systems (IROS)*, pp. 889 –894, 2007.
8. J. Jayender, M. Azizian, and R. Patel, "Bilateral telemanipulation of a flexible catheter in a constrained environment," in *IEEE International Conference on Robotics and Automation (ICRA)*, pp. 649 –654, 2008.
9. Northern Digital Inc., <http://www.ndigital.com/medical/aurora-techspecs.php>.
10. J. Green, R. Omari, B. Schirf, R. Tang, B. Lu, J. Gehl, J. Huang, J. Carr, F. Pereles, and D. Li, "Comparison of x-ray fluoroscopy and interventional magnetic resonance imaging for the assessment of coronary artery stenoses in swine," *Magnetic Resonance in Medicine* **54**(5), pp. 1094–1099, 2005.
11. W. Q. Zhang, K. R. Dai, and C. T. Wang, "Novel method for correction of x-ray fluoroscopic image," in *27th Annual International Conference of the Engineering in Medicine and Biology Society, IEEE-EMBS*, pp. 6340 – 6343, 2005.
12. Z. Zhang, "A flexible new technique for camera calibration," *IEEE Transactions on Pattern Analysis and Machine Intelligence* **22**, pp. 1330–1334, 2000.
13. M. Grass, R. Koppe, E. Klotz, R. Proksa, M. H. Kuhn, H. Aerts, J. O. de Beek, and R. Kemkers, "Three-dimensional reconstruction of high contrast objects using C-arm image intensifier projection data," *Computerized Medical Imaging and Graphics* **23**, pp. 311–321, 1999.
14. H. Zhang, F. Banovac, A. White, and K. Cleary, "Freehand 3D ultrasound calibration using an electro-magnetically tracked needle," *Medical Imaging 2006: Visualization, Image-Guided Procedures, and Display* **6141**(1), SPIE, 2006.
15. E. Trucco and A. Verri, *Introductory techniques for 3-D computer vision*, Englewood Cliffs, NJ: Prentice-Hall, 1998.
16. S. Krueger *et al.*, "Modality-integrated magnetic catheter tracking for x-ray vascular interventions," *Physics In Medicine And Biology* **50**, pp. 581–597, 2005.
17. C. K. Chui and G. Chen, *Kalman Filtering with Real-Time Applications*, Springer-Verlag, third ed., 1998.